Physica B 715 (2025) 417545

Contents lists available at ScienceDirect

Physica B: Condensed Matter

journal homepage: www.elsevier.com/locate/physb

Cost-effective synthesized Ce-doped ZnO nanoflowers for efficient photocatalytic dye degradation

Ümmühan Akın [a], Hamide Avcı [a], Raşit Aydın [a,*], Abdullah Akkaya [b], Osman Kahveci [c], Bünyamin Şahin [d,e], Enise Ayyıldız [c]

[a] Department of Physics, Faculty of Sciences, Selcuk University, Konya, Turkey
[b] Mucur Technical Vocational Schools, Tech. Prog. Department, Kırşehir Ahi Evran University, Kırşehir, Turkey
[c] Department of Physics, Faculty of Sciences, Erciyes University, Kayseri, Turkey
[d] Department of Basic Sciences, Faculty of Engineering, Necmettin Erbakan University, Konya, Turkey
[e] Department of Electrical and Computer Engineering, North Carolina State University, Raleigh, NC, USA

ARTICLE INFO

Keywords:
Photocatalytic degradation
ZnO nanoflowers
Rare earth
Cerium
Doping

ABSTRACT

In this study, we present the synthesis and characterisation of Ce-doped ZnO nanostructures utilizing the SILAR approach. The effect of Ce-doping on the structure, optical, electrical, and photocatalytic activity of ZnO nanoflowers was investigated in detail. Microscope images confirmed that the ZnO nanoparticles had a nanoflower-like shape. Mapping analysis confirmed that the Ce ions were uniformly distributed in the ZnO matrix. The incorporation of Ce influenced the material's surface features, leading to an increase in surface roughness. The diffraction result showed that the size of the crystals increased from 57.3 to 60.3 nm with 5.0 % Ce-doping. The FTIR spectra of the samples showed the Ce–O bonds in the region of 510–1000 cm^{-1}. Systematic reduction of the band gap from 3.24 to 3.05 eV was observed with increasing concentration of Ce from 0.0 to 5.0 %. It was also found that the surface roughness also affected the electrical properties and increased the specific contact resistance with Ce doping. Furthermore, the photocatalytic activity of the nanoparticles was also investigated for the degradation of methylene blue under UV-light irradiation. The turnover number and turnover frequency were also determined to rank the catalytic activity of the fabricated nanoparticles. The results indicated that 3.0 % Ce-doping enhanced the photocatalytic activity and degraded 95.8 % MB within 120 min. These findings indicate that cerium-doped ZnO shows great potential as an effective material for environmental purification processes.

1. Introduction

With the growth in industrialization worldwide, environmental pollution problems have also increased rapidly in recent years. It is well known that organic/inorganic pollutants used in industry are important to water pollution. Even low amounts of exposure to these hazardous pollutants can cause permanent genetic problems that last for generations [1]. Therefore, more studies are needed to minimize these potentially life-threatening factors, even if we cannot eliminate them. Recent advancements in photocatalytic materials have attracted considerable interest owing to their prospective applications in environmental remediation, especially in the degradation of organic contaminants [2–6]. Despite the increasing interest, comprehensive studies on advanced photocatalytic materials, especially on their effectiveness in environmental remediation, are still needed. Metal oxide materials have consistently been a primary focus of photocatalysis research owing to their distinctive chemical and physical features, rendering them appropriate for many environmental and energy-related applications [7–10]. Semiconducting metal oxides, including titanium dioxide (TiO_2), tungsten oxide (WO_3), and zinc oxide (ZnO), exhibit significant promise in the breakdown of organic contaminants, water splitting, and various photochemical reactions. ZnO has emerged as an up-and-coming contender because of its exceptional chemical stability, superior photocatalytic efficiency, and capacity to produce reactive species when exposed to ultraviolet light [11–13].

ZnO is an exceptionally appealing photocatalyst due to its distinctive combination of physical and chemical characteristics. ZnO is a wide-bandgap semiconductor (about 3.37 eV) with a substantial exciton

* Corresponding author.
E-mail address: raydin@selcuk.edu.tr (R. Aydın).

https://doi.org/10.1016/j.physb.2025.417545
Received 28 April 2025; Received in revised form 4 June 2025; Accepted 28 June 2025
Available online 30 June 2025

binding energy (60 meV), enabling effective charge carrier production under ultraviolet (UV) illumination. The hexagonal wurtzite crystal structure offers a substantial surface area and superior thermal and chemical resilience, rendering it appropriate for prolonged environmental applications. ZnO exhibits exceptional optical characteristics, including elevated transmittance in the visible spectrum and robust UV absorption, which augment its photocatalytic capabilities [14–16]. ZnO's broad bandgap, elevated exciton binding energy, and environmental resilience make it a multifaceted material with many uses. In optoelectronics, ZnO is the material of choice for ultraviolet light-emitting and laser diodes due to its effective light emission and thermal stability [17,18]. Furthermore, ZnO is vital in sensors, particularly gas sensors, due to its exceptional sensitivity to chemical and environmental changes [19]. In the field of energy, ZnO is an indispensable material. It is a transparent conductive oxide in solar cells, enhancing efficiency while ensuring longevity [20]. Its photocatalytic characteristics are extensively utilized in environmental applications, including water filtration and the destruction of organic contaminants [21]. ZnO's antimicrobial and biocompatible characteristics make it optimal for medical applications such as wound healing, sunscreens, and antibacterial coatings [22].

ZnO materials are produced by a variety of techniques, including sol-gel, hydrothermal, chemical vapor deposition, physical vapor deposition, combustion synthesis, solid-state reactions, and Successive Ionic Layer Adsorption and Reaction (SILAR), which are selected according to the specific applications or desired material properties [23–27]. Among these methods, one of the most important advantages of SILAR is its ability to produce uniform and well-bonded films at low temperatures, which makes it suitable for various substrates, including flexible materials. Furthermore, SILAR allows precise control over film thickness by adjusting the number of deposition cycles, and its simplicity and cost-effectiveness make it an attractive option for large-scale applications [28–30].

Cerium (Ce), a rare-earth element, has been the subject of considerable interest as a dopant for ZnO, mainly because of its distinctive electronic configuration and redox properties. The doping of ZnO with rare-earth elements, such as Ce, has been identified as an effective strategy for improving its optical and electronic properties. The unique electronic configuration and redox flexibility of cerium have been demonstrated to influence the bandgap energy and defect density in semiconductor systems, thereby enhancing light absorption and charge separation. The introduction of Ce into the bandgap of ZnO results in the formation of localised states, which reduces the recombination rate of charge carriers and extends the light absorption of ZnO into the visible region. This is a highly favorable process for photocatalysts powered by visible light, making Ce-doped ZnO a promising material for advanced photocatalytic applications [31–34]. The ability to modify the characteristic parameters of materials as desired by the doping process has focused researchers on different studies. Experimentally, the characterization of structural, electrical, magnetic properties and linear/non-linear optical behaviors of Ce-doped ZnO structures prepared using different growth methods have been carried out by many researchers such as Wang et al. [35], Fifere et al. [36], Chattopadhyay et al. [37]. Theoretical studies also supported experimental studies. The band structures and optical properties of Ce-doped ZnO crystal were investigated by Wen et al. [38] using the first principles method. Rodriguez-Mena et al. [39] performed a study on the electronic structure of Ce-doped ZnO using density functional theory. They showed that the relative position of the Fermi level can play an important role in explaining the higher photocatalytic activity for the structure.

This presented study aimed to improve the characteristic properties of nanostructures prepared with different doping ratios and, especially, to design an optimum photocatalytic process. For this purpose, undoped and Ce-doped ZnO films have been synthesized on glass substrates using the SILAR method. To comprehensively evaluate the effect of Ce doping on the optical, electrical, and photocatalytic properties, the ZnO was doped with different Ce concentrations. The photocatalytic efficacy of these materials was evaluated utilizing methylene blue, a prevalent model contaminant, under regulated settings. The novelty of our work lies in introducing a new application-oriented approach based on scalable SILAR production, precise doping control, and comprehensive evaluation of structural, optical, electrical, and photocatalytic properties. The comprehensive analyses of the films are outlined in the subsequent sections.

2. Experimental section

Undoped and Ce-doped ZnO nanofilms and nanopowders were prepared using SILAR, a solution-based growth technique. The synthesis bath solution comprised zinc acetate dihydrate (Molecular Formula: $C_4H_{10}O_6Zn$) and deionised (DI) water. The pH of the growth solution was measured to be approximately 10.0 after adding NH_4OH, heating to 365 K, and mixing with a magnetic stirrer at 550 rpm. Cerium (III) nitrate hexahydrate (Molecular Formula: $CeH_{12}N_3O_{15}$) was used to synthesize Ce-doped ZnO materials using the same technique. Three materials (0.0 %, 3.0 %, and 5.0 %) were grown to investigate the effect of the rare-earth element Ce as a dopant on the main physical properties and photocatalytic performance of nano-sized ZnO flower-like powders and films. The annealing temperature employed in this experiment was 550 K for 45 min. Fig. 1 illustrates the schematic representation of the deposition process for ZnO, ZnO:Ce (3.0 %), and ZnO:Ce(5.0 %) films and powders.

Undoped and Ce-doped ZnO materials were examined to assess their morphological, structural, optical, and electrical properties and their photocatalytic performances, employing various characterization techniques. The particle size, shape, and distribution of nanostructured ZnO flowers were analyzed using scanning electron microscopy (SEM; Zeiss evo Ls 10) and atomic force microscopy (AFM; NT-MDT/Ntegra Solaris) techniques. The elemental compositions of the samples were ascertained by energy-dispersive X-ray spectroscopy (EDX). The phases of the synthesized materials were analyzed using an X-ray diffractometer (Bruker D8 Advance) equipped with a Cu Kα radiation source ($\lambda \pm 1.54056$ Å). The functional groups were characterized using Fourier transform infrared (FTIR) spectroscopy (Bruker Vertex70). The Jasco V-670 UV–Vis spectrophotometer was employed to examine the optical properties. Current-voltage (I-V) measurements for the electrical analysis were conducted utilizing a Zive Sp1 (Wonatech) Potentiostat. The deposition of Au metal for contacting thin film samples was carried out by the physical evaporation deposition method using a shadow mask with a unique geometry under a high vacuum (1×10^6 mTorr). Measurements were taken at a scanning rate of 1 mVs^{-1} in the applied voltage range of −5 V to +5 V.

The photocatalytic activity of undoped and Ce-doped ZnO thin films was evaluated by monitoring the degradation of methylene blue (MB) under controlled UV light irradiation. A fresh 10 ppm MB solution was prepared in distilled water, and its pH was adjusted to 10 by using NaOH to ensure consistency. For each experiment, 30 mg of the photocatalyst was immersed in 30 mL of the MB solution (catalyst loading: 1 g/L) and stirred in the dark for 20 min to achieve adsorption-desorption equilibrium. Preliminary dark adsorption tests confirmed no further significant dye adsorption occurred beyond this period.

The mixture was irradiated under a 3 W UV LED lamp (emission peak: 395–400 nm, and intensity was approximately 7 mW/cm^2) positioned 10 cm below the reaction vessel. Aliquots (3 mL) were collected at 10-min intervals over a total irradiation time of 120 min. Each aliquot was immediately centrifuged at 3000 rpm for 4 min to remove catalyst particles, and the supernatant's absorbance was measured at 665 nm using a Shimadzu UV-1201 spectrophotometer (calibrated with a blank MB solution of known concentration).

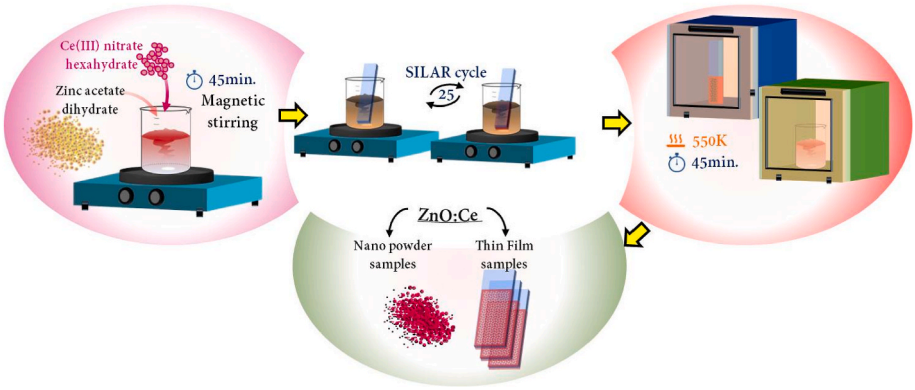

Fig. 1. The schematic representation of the SILAR method for depositing nanostructured undoped and Ce-doped ZnO films and nanopowders.

3. Results and discussion

3.1. Morphological analyses

The morphological characteristics of ZnO films were examined using SEM to assess the impact of Ce doping at concentrations of 3.0 % and 5.0 %. Fig. 2 displays SEM images of undoped and Ce-doped ZnO materials, showing that undoped ZnO films have a consistent hexagonal nanoflower-like structure. There are similar SEM results of flower-like structure for samples in previous works [40–42]. Ce supplementation at concentrations of 3.0 % and 5.0 % induced significant alterations in morphological features. The surface structure of ZnO films became denser and firmer with Ce doping. While the nanoflowers were thicker in undoped ZnO, the nanoflower structures became thinner with rare-earth Ce doping. The alterations in morphology with increasing Ce content demonstrate the susceptibility of ZnO's structural characteristics to

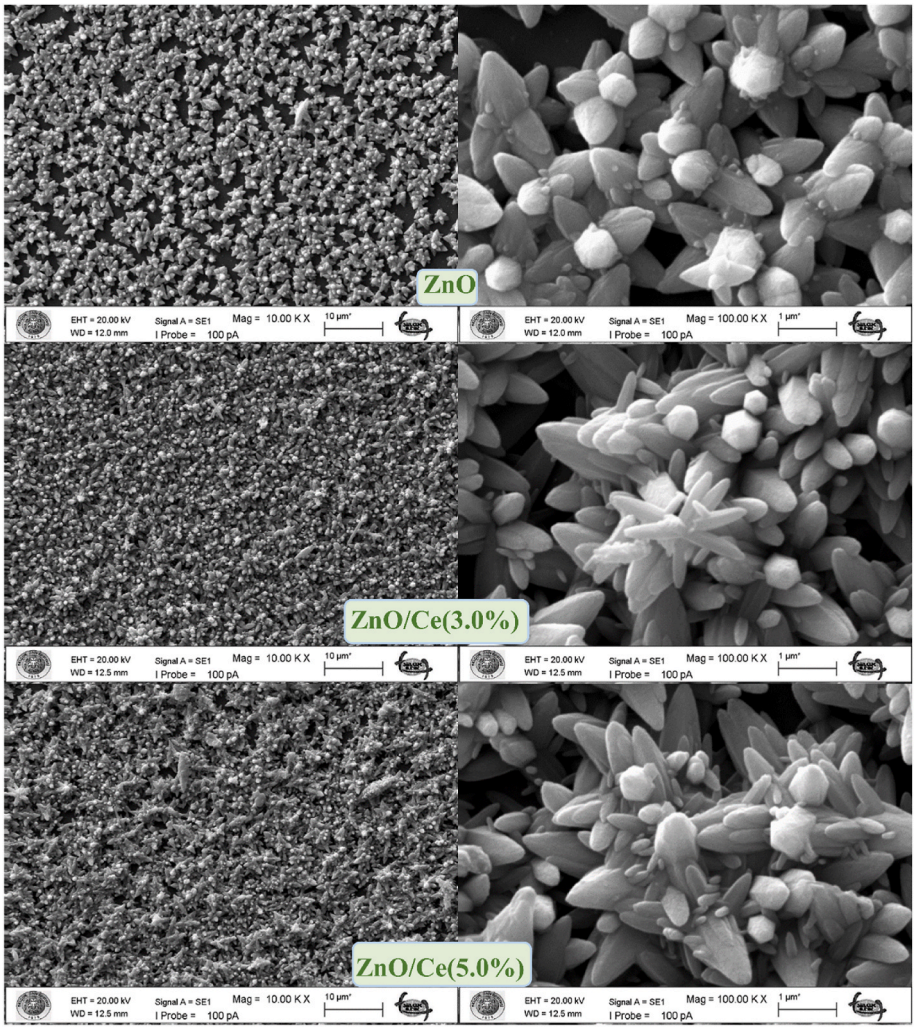

Fig. 2. SEM images of nanostructured ZnO thin films produced at different Ce doping concentrations. SEM scans indicate that all ZnO films exhibit a uniform hexagonal nanoflower morphology.

doping. These changes in surface morphology may be due to Ce doping altering the nucleation and growth processes during ZnO synthesis and the formation of defects such as oxygen vacancies and interstitial regions with Ce addition to ZnO. Moreover, these alterations are linked to the substitutional integration of Ce ions within the ZnO lattice, resulting in lattice strain and influencing crystal growth [43–46]. The impact of doping was examined by estimating the average particle size of the samples using a pixel analysis program. The samples' average particle sizes are found to be 778, 485, and 400 nm for the undoped, 3.0 %, and 5.0 % Ce-doped ZnO films, respectively. It has been observed that particle size decreases with increasing Ce content. This decrease may be related to Ce ions occupying grain boundaries or surfaces, preventing particles from bonding with each other, and changes in surface energy.

Energy-dispersive X-ray (EDX) mapping was conducted to analyze the elemental distribution and verify the integration of cerium (Ce) into the ZnO structure. The presence of Zn, O, and Ce in ZnO nanostructures doped with 3.0 % Ce was corroborated by the peaks illustrated in Fig. 3. Furthermore, Fig. 3 includes a table that delineates the weight percentage of different components in the ZnO/Ce (3.0 %) sample. After doping with 3.0 % Ce, EDX mapping showed that Ce ions were successfully incorporated into the structure and evenly distributed throughout the surface. Fig. 3 presents mapping images that illustrate the presence of Zn (blue), O (green), and Ce (red) in the ZnO/Ce film, hence verifying the successful doping of Ce.

AFM was utilized to assess the influence of Ce-doping on the surface morphology of ZnO films, focusing on average roughness (Sa), root mean square roughness (Sq), and entropy. Fig. 4 presents 2D and 3D AFM images of undoped and Ce-doped ZnO structures. The AFM results demonstrate that Ce doping markedly influences the surface morphology, as indicated by increases in Sa, Sq, and entropy values. The undoped ZnO sample exhibited Sa and Sq values of around 151.675 nm and 193.785 nm, respectively, indicating a relatively smooth surface. With the introduction of 3.0 % Ce, the values rose to 190.25 nm for Sa and 235.592 nm for Sq, signifying a transition towards a rougher surface morphology. At 5.0 % Ce doping, the Sa and Sq values increased to 211.18 nm and 260.223 nm, respectively, underscoring the substantial effect of elevated Ce incorporation on surface roughness. The entropy values consistently rose, increasing from 12.828 for undoped ZnO to 13.098 for 3.0 % Ce-doping, culminating at 13.229 for 5.0 % Ce-doping. The elevation in Sa, Sq, and entropy values with increasing Ce content can be ascribed to multiple interconnected processes. This strain leads to inconsistent crystal growth, resulting in uneven surface characteristics and increased roughness parameters. Furthermore, adding Ce alters the nucleation and growth dynamics, frequently resulting in defect-rich areas and aggregation at elevated doping concentrations. The rise in entropy is associated with the random arrangement of Ce ions and the resulting structural irregularities, which disturb the uniformity of the ZnO surface [47–50].

3.2. X-ray diffraction analysis

The XRD analysis identified the phases of the ZnO films that were produced. Fig. 5 presents a comparative analysis of the XRD images for undoped and Ce-doped ZnO (3.0 % and 5.0 %) materials. The observed peaks align closely with the established pattern (JCPDS No: 89–0510) corresponding to the ZnO phase, which crystallizes in a wurtzite (hexagonal) structure [51]. No diffraction peaks were detected for any of the other impurities. Three prominent diffraction lines are observed at angles of 31.91°, 34.57°, and 36.39°, corresponding to the ZnO lattice planes of (100), (002), and (101), respectively. The diffraction pattern displays the emergence of additional peaks at 47.66°, 56.70°, 62.96°, 66.46°, 68.03°, 69.17°, 72.65° and 77.02°, which can be attributed to the (102), (110), (103), (200), (112), (201), (004) and (202) planes of the ZnO particles, respectively. Fig. 5 illustrates that the peak intensity,

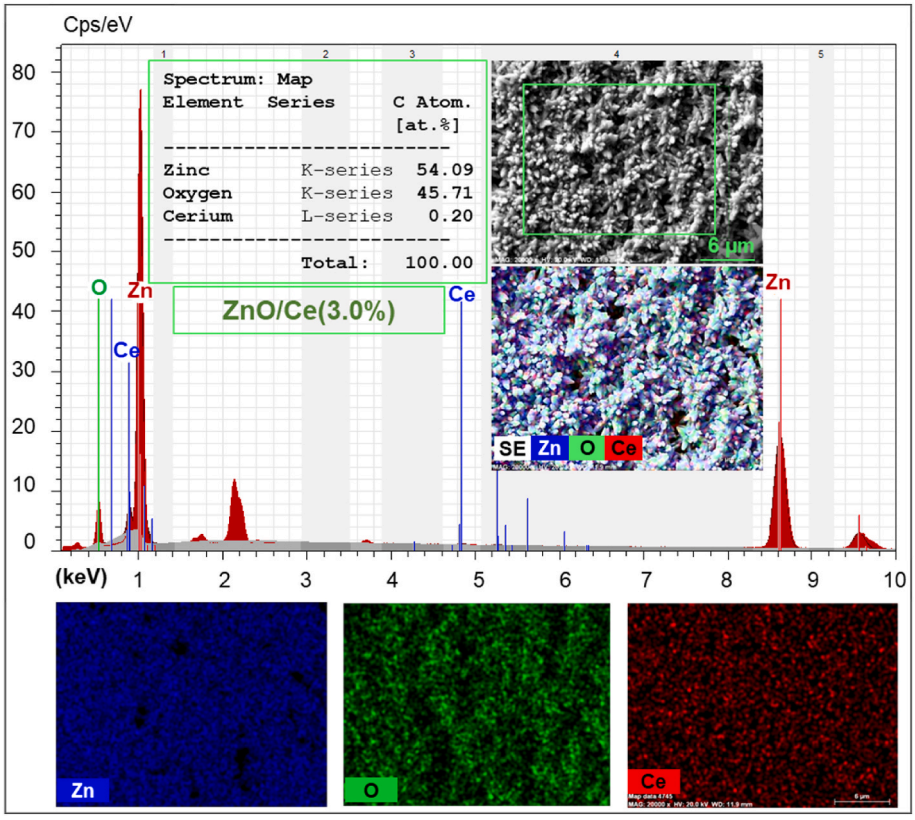

Fig. 3. Analyses of elemental mapping for the nanostructured ZnO samples fabricated using the SILAR method at varying concentrations of Ce doping. The mapping images validate the effective doping of Ce.

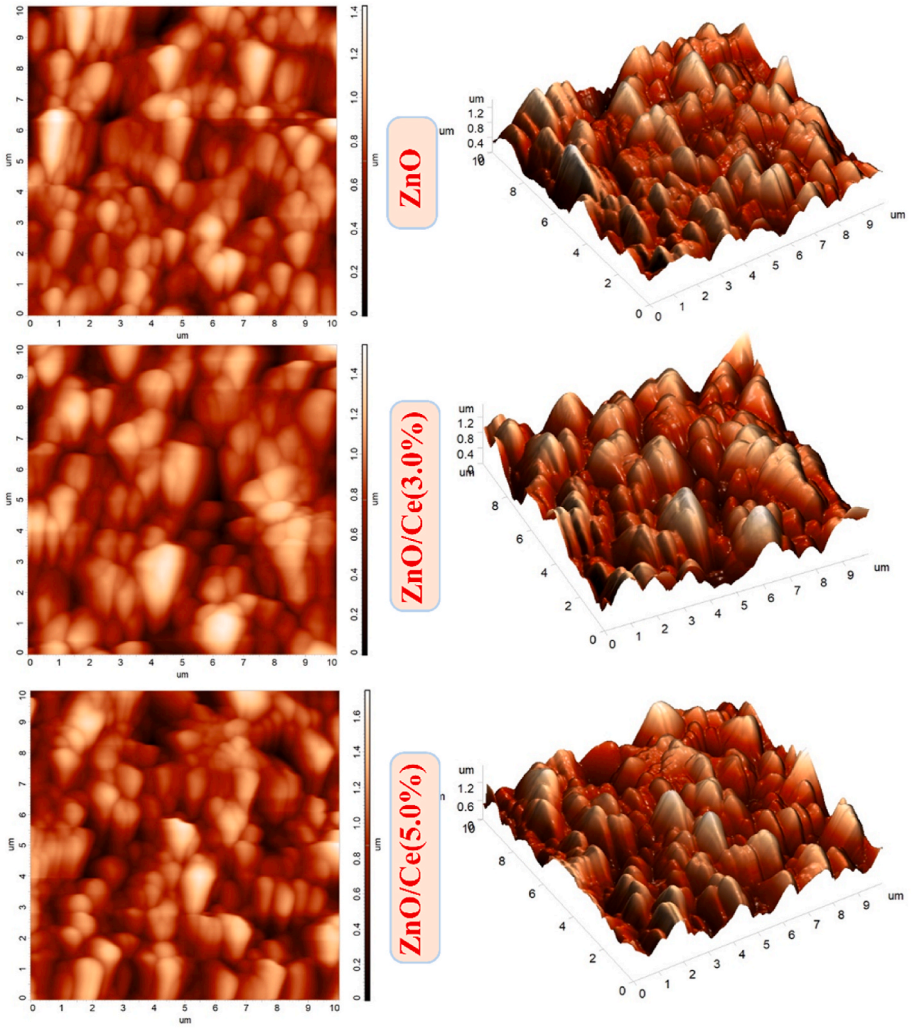

Fig. 4. 2D and 3D AFM images of nanostructured ZnO thin films SILAR produced with varying cerium doping concentrations over a scan area of 10 μm × 10 μm. The alteration in the morphology of the films due to Ce-doping is evident in the variations in surface roughness among the samples.

or crystallinity, declines in conjunction with an increase in the concentration of the Ce dopant. This decrease in the peak intensities observed in the XRD patterns of ZnO films with increasing Ce doping concentrations can be attributed to the lattice strain caused by the ionic radius mismatch between Ce^{3+} (1.01 Å) and Zn^{2+} (0.74 Å) upon incorporation of Ce ions into the ZnO lattice, and the disruption of the periodicity of the crystal structure [52,53].

The average size of the crystallites (D) was calculated using the Scherrer equation [54] based on the full width at half maximum (FWHM) (β) values of the XRD peaks.

$$D = \frac{K\lambda}{\beta \cos\theta} \tag{1}$$

In this context, D, λ, and θ denote the crystallite size, the wavelength of X-ray radiation (λ = 1.54056 Å) for Cu-Kα, and the Bragg angle, respectively. The average D of undoped and Ce [3.0 % and 5.0 %] doped ZnO nanoparticles were 57.3 nm, 58.9 nm, and 60.3 nm, respectively. This change in D may be due to the effect of Ce ions on the nucleation and growth processes during the formation of ZnO crystals. It may also be based on the fact that the addition of Ce can affect the thermal stability of the ZnO matrix, especially at elevated temperatures, and the unique redox properties of Ce can alter the reaction kinetics [55,56].

3.3. FTIR analysis

The FTIR spectra of ZnO films doped with Ce at varying concentrations offer insight into the doping-induced vibrational characteristics and chemical alterations. Fig. 6 shows the FTIR spectra of undoped, 3.0 %, and 5.0 % Ce-doped ZnO nanoflowers in the 400-4000 cm^{-1} region. The 400-600 cm^{-1} absorption band corresponds to metal-oxygen stretching vibration modes. The bands at 1000 cm^{-1} and 510 cm^{-1} may be due to Ce-O stretching vibration. These peaks confirm the successful incorporation of Ce ions into the ZnO matrix via doping. The bands observed at 1400-1600 cm^{-1} correspond to the C=O stretching, potentially indicating organic species remaining from the synthesis process. The broad absorption bands in the 3000-3600 cm^{-1} regions are associated with O-H stretching vibrations from hydroxyl groups [57–59].

3.4. Optical analysis

It is important to understand how doping the rare element Ce into ZnO with a broad and direct band gap [60] affects photocatalytic activities, for which the absorption characteristics and the optical band gap are crucial. The effect of doping on the energy band gap has been investigated using the Tauc relation [61]:

$$(\alpha h\upsilon) = B\left(h\upsilon - E_g\right)^m \tag{2}$$

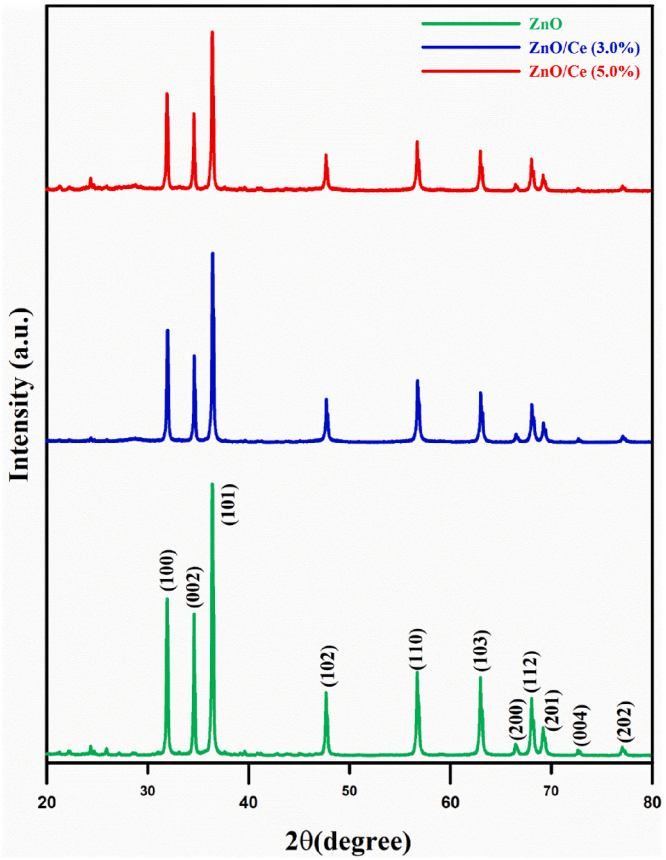

Fig. 5. X-ray diffraction patterns of nanostructured ZnO thin films produced with varying concentrations of Ce doping. The peak intensity, indicative of crystallinity, slightly decreases as the percentage of Ce increases.

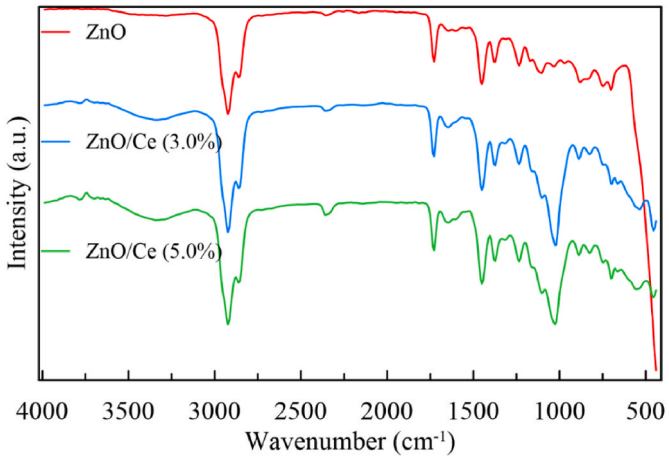

Fig. 6. FTIR spectroscopy of ZnO thin films synthesized with varying cerium doping levels. The 1000 and 510 cm^{-1} peaks indicate that Ce ions have been successfully incorporated into the ZnO matrix via doping.

E_g, α, h, υ and B are the band gap energy, absorption coefficient, Planck's constant, incident photon frequency, and proportionality constant, respectively. Additionally, the parameter m in the aforementioned expression is a constant, corresponding to 1/2 for direct transition. To determine the band gaps, $(ah\upsilon)^2$ was plotted against $(h\upsilon)$ as shown in Fig. 7, and from the extrapolation of the linear region to the energy axis $(h\upsilon)$, the energy band gap values of the undoped and 3.0 % and 5.0 % Ce-doped ZnO films were determined to be 3.24 eV, 3.11 eV, and 3.05 eV, respectively. Doping Ce ions at different ratios in ZnO semiconductor material causes a significant decrease in the optical band gap. Doping causes modification in the bandgap of semiconductors due to the formation of trap centers and crystal defects in the structure [60,62]. Additionally, the presence of Ce ions in the ZnO structure creates localized states in the optical band gap of ZnO [63,64]. Localized energy states arise from many factors such as microstructural changes, lattice strains, defects caused by oxygen vacancies, and the density and size of doping ions [62,64–66]. Localized energy states are very close to the conduction band. This leads to a decrease in the band gap and, thus, shifts the absorption towards longer wavelengths [64,65]. The films prepared in the presented study exhibited a spectrum where the absorption edge slightly shifted towards lower energies, i.e., towards red in the visible region, with increasing Ce doping ratio. Different researchers have also reported this observed situation. Liu et al. [67] emphasized that the shift of the absorption edge towards longer wavelengths and the narrowing of the band gaps can be explained by the numerous surface defects formed in the structure, such as Zn interstitials and oxygen vacancies. They pointed out that the defects formed may enhance the photocatalytic activity of Ce-doped ZnO materials. Vijayaprasath et al. [68] stated that this observed change is strongly related to the quantum confinement effect and the formation of impurity levels within the band gap of ZnO. In another study, Chang et al. [69] observed that the undoped ZnO band gap of 3.35 eV decreased to 3.10 eV with increasing Ce-doping amount. In addition, the observed decrease in band gap with doping was reported by Sharma et al. [70], Liang et al. [71], and Kasar et al. [72]. As a result, doping plays an essential role in the energy band gap and photocatalytic behavior.

The UV–Vis absorption spectra of ZnO films with and without Ce are shown in Fig. 8. As can be seen from the graph, Ce doping significantly affects the optical absorption behaviour of ZnO. The undoped ZnO film exhibits a sharp absorption edge in the near-UV region, which is characteristic of its wide direct bandgap. However, with the addition of Ce at ratios of 3.0 % and 5.0 % to the ZnO structure, the absorption intensity in the UV and visible regions increases significantly and the absorption edge shifts towards longer wavelengths (red shift). This red shift is consistent with a decrease in the optical band range and can be linked to various physical mechanisms. Incorporating Ce ions into the ZnO lattice may cause the formation of local defect states, such as oxygen vacancies and Ce^{4+}/Ce^{3+} interstitial sites. The size difference between Ce and Zn atoms may cause lattice distortions and strain effects, leading to changes in the electronic structure and thus changes in the absorption spectrum [73–75].

3.5. Electrical analysis

The electrical properties of ZnO/Ce thin films are investigated by depositing Au onto the surface of the thin films with a shadow mask. The transfer length method (TLM) is used for contact resistance measurement. Photographic and schematic representations of Au pad patterns for contact resistance measurement are included in Fig. 9a, where they are embedded in the graph. The length l and width w of Au pads are equal to 7.00 mm and 0.35 mm, respectively. The I–V characteristics of Au metal contact to ZnO/Ce thin films at the different Ce doping levels are shown in Fig. 9a. The voltage is varied from −5 to 5 V, and the current is recorded with a Potentiostat device, as shown in this Fig. 9 where the voltage is applied to pads 1–2. Ce doping increases the slope in the I-V curve; the slope is the highest at 3.0 %. The contact resistance is high due to the oxide's nature and the poor metal/metal oxide interface [76]. However, the total resistance (R_T) value of ZnO thin film decreases with Ce doping, and the smallest R_T value is equal to 2.83×10^6 Ω for 3.0 % Ce doping (contact from pads 1–2). Ce-doping probably leads to an increase in the carrier density (the highest at 3.0 % Ce), which reduces the potential barrier to electron flow at the Au/ZnO contact interface and increases the conductivity of the ZnO thin film.

The linear behavior of the I–V curve of Ce-doped ZnO thin films

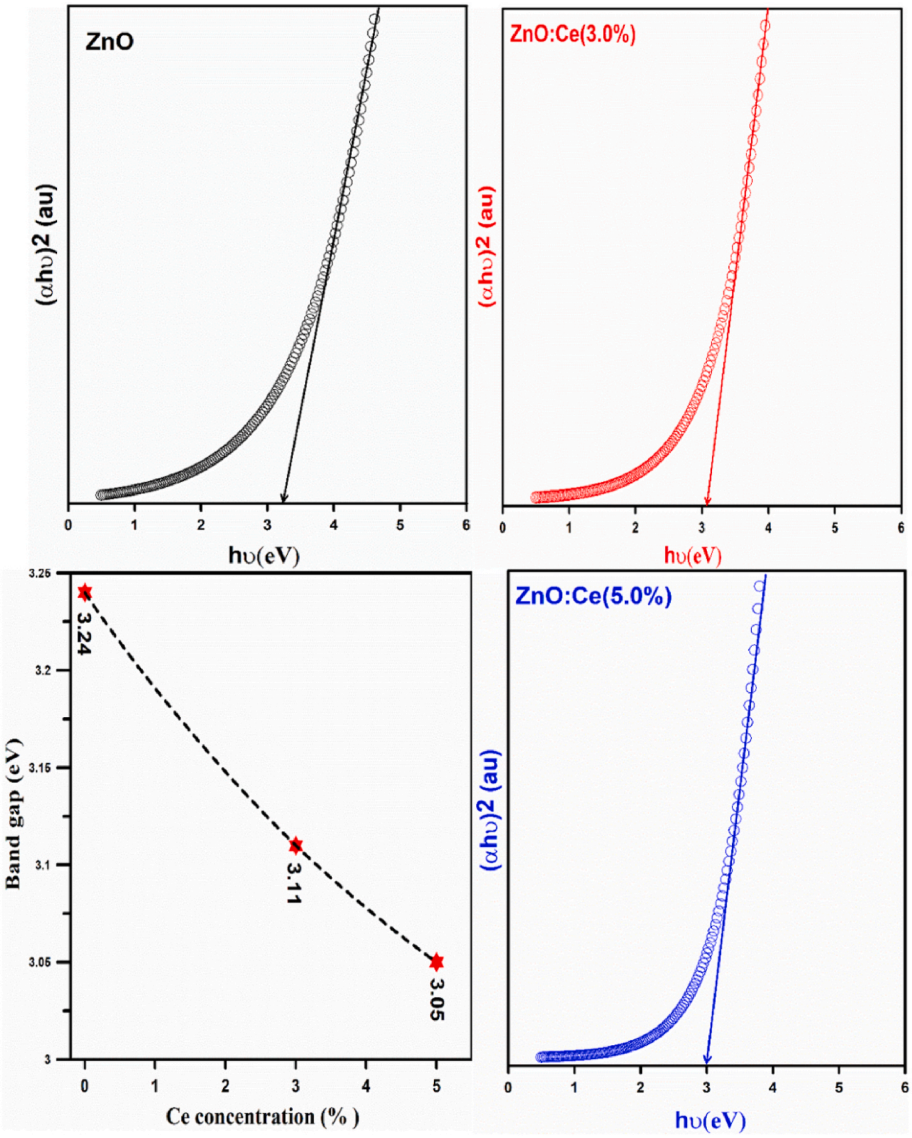

Fig. 7. Graph of Tauc's law illustrates the relationship between the absorption coefficient, α, and photon energy, $(h\upsilon)$, for Ce-doped ZnO sheets with varying Ce concentrations.

shows an improved ohmic property compared to the undoped ZnO thin films. The slope of the I–V plot increases as the inter-pad distance decreases, i.e., the R_T value increases with increasing pad distance. The I-V characteristics of the contacts taken from different pads of the 3.0 % Ce-doped ZnO thin film are given in Fig. 9b.

R_T value between the Au pads (1–2 (R_1), 2–3 (R_2), and 3–4 (R_3)) deposited on the ZnO/Ce thin films (for metal/thin film contact) is plotted as a function of the distance (d) between the pads as shown in Fig. 10. From this graph, the ZnO/Ce thin film sheet resistance (R_{Sh}) under the Au pad contacts (from the slope), the total contact resistance (R_C), and effective transfer length (L_{Ef}) (from the intercept) can be determined. Detailed information about this method has been reported previously [77–79]. After determining these data with the help of the graph, the specific contact resistance (ρ_C) is calculated using Equation (3).

$$\rho_C = R_C L_{Ef} w \tag{3}$$

Fig. 10a, b, and c show the R_T-d graphs for ZnO and ZnO/Ce samples. The related fit equations are embedded in these graphs. The electrical parameters calculated for ZnO/Ce thin films are summarized in Table 1.

The effect of Ce doping on the total contact resistance values exhibits a change similar to the total resistance. Again, the lowest R_C value is 3.0 % Ce doping and 1.23×10^6 Ωcm^2. The specific contact resistance between the metal pads and the metal oxide structure helps analyze ohmic behavior. ρ_C values increase with Ce doping. Surface roughness is essential to the value of material performance. The ρ_C value is expected to be lower on smoother surfaces [79]. This situation is entirely consistent with the AFM and SEM results. The surface roughness of ZnO thin films increases with Ce doping. Many factors, such as carrier concentrations, defects, oxygen affinity, and crystal quality, may affect ρ_C [80]. These situations also affect the barrier height and surface conditions of ZnO.

It is known that factors affecting electrical conductivity, such as carrier density, also affect photocatalytic behavior. It is concluded that Ce doping affects the electrical properties of ZnO thin films. Total resistance values decrease with Ce doping; the lowest resistance is observed at 3.0 % Ce, and its value increases slightly at doping above this rate, but it is still lower than that of undoped ZNO. This shows that the metal (Au) and metal oxide (ZnO/Ce) contact exhibits different electrical properties depending on Ce doping.

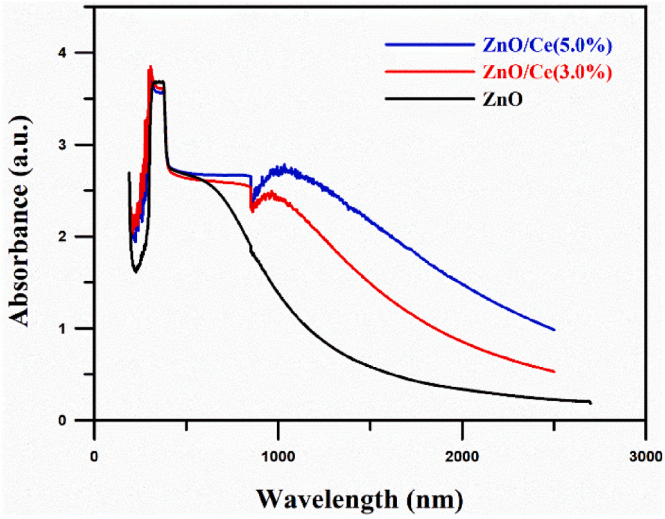

Fig. 8. Optical absorbance spectra of ZnO films produced with varying concentrations of Ce doping.

3.6. Photocatalytic efficiency analysis

The degradation mechanism can be summarized in three steps (Fig. 11) [81–85]. In the first step, e^-/h^+ pair, created by uv-light-assisted excitation of metal oxide, takes part in the formation of superoxide and hydroxyl radicals. In the second step, excited electrons reduce oxygen molecules to superoxide radicals ($\bullet O_2^-$), while holes contribute to water oxidation, forming hydroxyl radicals (•OH). Finally, these reactive oxygen species then oxidize methylene blue, leading to its degradation into non-toxic byproducts.

The ZnO acts as a photocatalyst under the irradiation of sunlight. This activity can also be easily observed in degrading dye concentrations under UV light at different time intervals. The yield of degradation or degradation efficiency (η) was obtained using Equation (4) [82–84]:

$$\eta = \left(C_0 - C_t/C_0\right) x100\% \quad (4)$$

C_0 is the initial concentration, and C_t is the concentration (mg/l) after irradiation at specific intervals. Fig. 12 demonstrates the photocatalytic behavior (a) and degradation efficiency (b) of the prepared ZnO and Ce-doped ZnO nanostructures. This figure exhibits the degradation of dye concentration at different time intervals.

As shown in Fig. 12b, the degradation efficiency of ZnO and Ce-doped ZnO gradually decreased. After 120 min of exposure to UV light, all samples' η values take below 75 %, and these values show that degradation kinetics were a first-order process, as shown in Fig. 13.

The degradation rate constant (k) was obtained from linear fit equations of first-order kinetic plots. These values were 0.028, 0.037, and 0.012 for ZnO and Ce-doped (3.0 % and 5.0 %) ZnO NPs, respectively [86]. The degradation rate and degradation rate constant of ZnO and Ce-doped (3.0 % and 5.0 %) ZnO nanostructures were very close; however, increasing Ce 3.0 % doping causes a slight decrease in this rate. This situation can be explained by changes in the formation of e^-/h^+ pairs due to the excess metal ions (Ce^{+4}).

Photocatalytic degradation can be well understood with the help of some metrics. Continuous degradation reactions in heterogeneous reaction environments are especially notable. Quantifying catalyst efficiency with some terms, such as "active site," "turnover number (TON)," and "turnover frequency (TOF)" can be very beneficial in understanding ongoing reactions. A quantitative measure of a catalyst's efficiency can be represented with TON, and this value is provided by dividing the total number of product molecules by the number of available active sites or catalyst molecules in the system [54,87–89].

$$\text{TON} = \frac{(\%\eta)(\text{Number of molecules of substrate})}{\text{Number of molecules of catalyst}} \quad (5)$$

Besides that, TOF values bring a dynamic evaluation of the catalytic performance of the catalyst and give several reaction cycles occurring over a set period [54,88].

$$\text{TOF} = \frac{\text{TON}}{\text{Time}} \quad (6)$$

In our experiment, 30 mg ZnO and Ce-doped ZnO samples were used and after 60 min of UV light exposure, the calculated photocatalytic degradation process parameters are given in Table 2.

Active site dopant arising from dopant Ce atoms measured 6.4 × 10^{-6} mol and 10.7 × 10^{-6} mol for 3.0 % and 5.0 % Ce-doped ZnO materials, respectively. The total active site number was about 37 mmol,

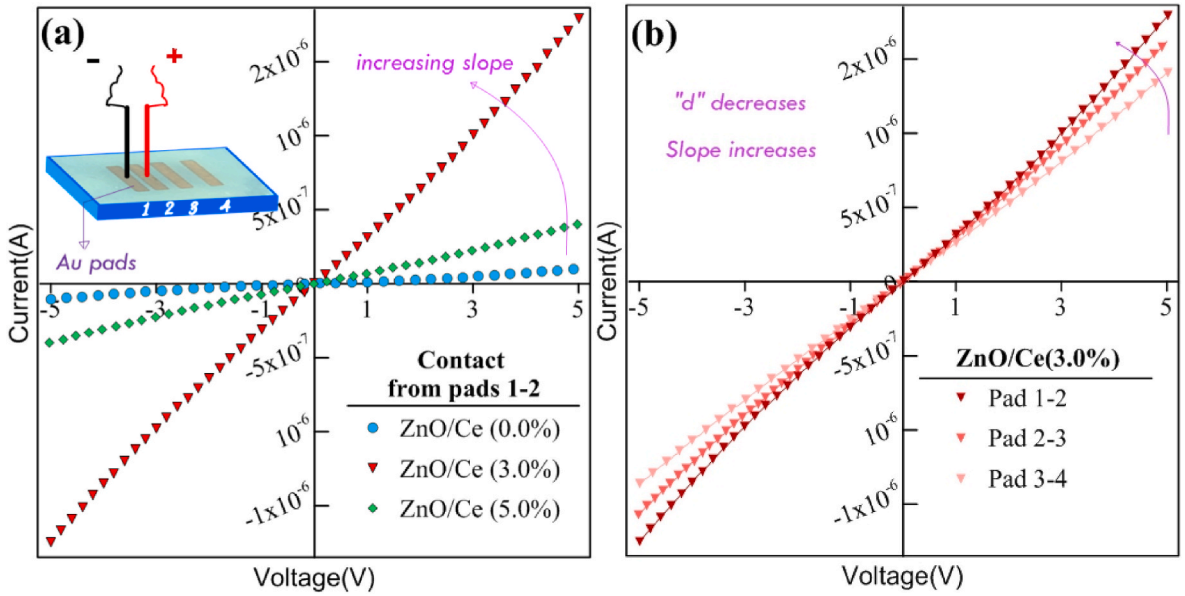

Fig. 9. a) I-V curve of ZnO/Ce thin films for 1–2 pads contact (embedded in the figure are photographic and schematic drawings of the Au pad patterns) and b) I-V curve from different pads for the 3.0 % Ce-doped ZnO thin film.

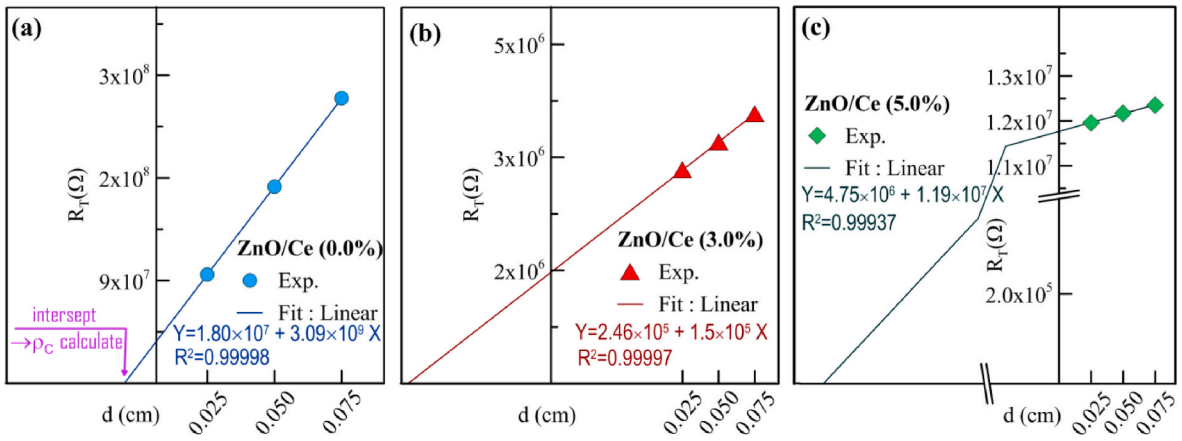

Fig. 10. Total resistance plots of a) ZnO/Ce (0.0 %), b) ZnO/Ce (3.0 %), and c) ZnO/Ce (5.0 %) thin films depending on pad distance (the slope of the plots and the intercept at $R_T = 0$ are used in the calculations of total and specific contact resistance).

Table 1
The electrical parameters of ZnO/Ce thin films from the TLM method.

Sample	R_T (Ω)			R_C (Ωcm^2)	ρ_C (Ωcm^2)
	R_1	R_2	R_3		
ZnO/Ce (0.0 %Ce)	9.54×10^7	1.72×10^8	2.50×10^8	8.99×10^6	0.65×10^6
ZnO/Ce (3.0 %Ce)	2.83×10^6	3.20×10^6	3.58×10^6	1.23×10^6	25.33×10^6
ZnO/Ce (5.0 %Ce)	1.20×10^7	1.21×10^7	1.22×10^7	5.93×10^6	94.71×10^6

and degradation efficiency was very high in the undoped and 3.0 % in the Ce-doped ZnO sample. Also, the active sites of the doping atoms were determined, and the doping level was considered. These calculated parameters slightly increased in both TON and TOF values when the doping concentration reached 3.0 % Ce-doping, indicating that the catalytic efficiency of ZnO NPs was boosted somewhat. However, when the Ce doping rate is 5.0 %, the degradation TON and TOF values decrease, although the total active sites are almost constant. Although Ce doping caused a red shift in the optical band gap, enhancing theoretical absorption in the visible range, photocatalytic activity was still evaluated under UV light due to the energy requirement for efficient electron–hole pair generation. For this reason, efficiency results have remained limited.

As shown in Table 3, the Ce-doped ZnO nanostructures synthesized

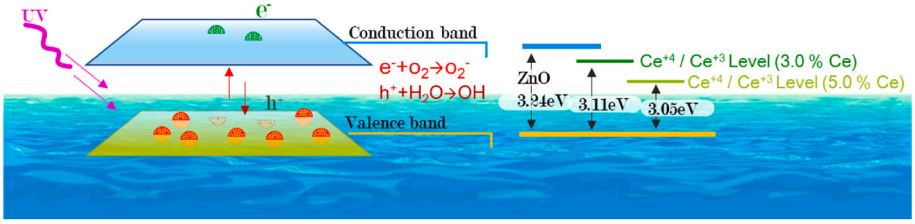

Fig. 11. Schematic representation of the photodegradation process and superoxide and hydroxyl radicals formation.

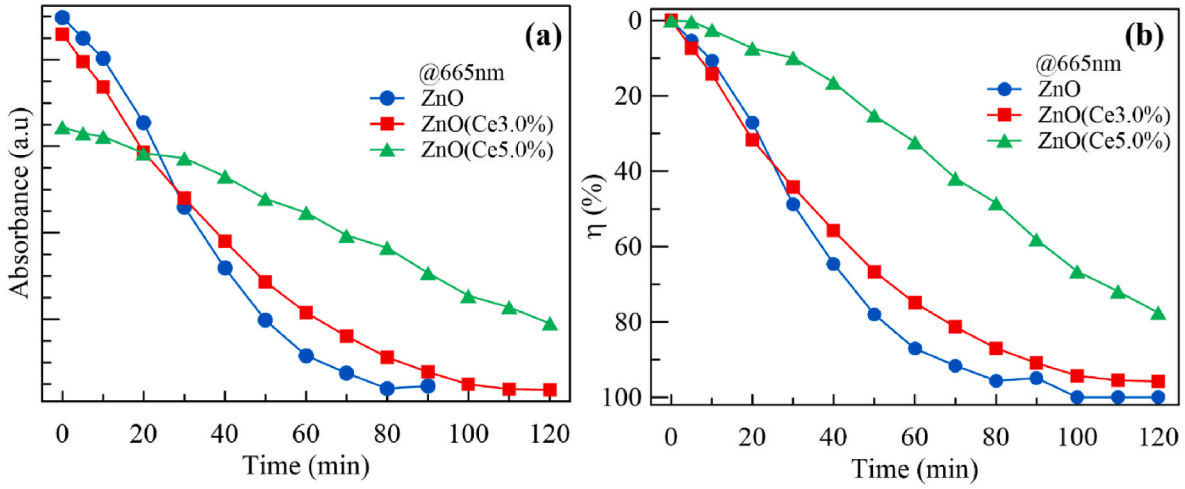

Fig. 12. Changes in absorbance values of MB solutions with UV light exposure time of ZnO and Ce-doped ZnO (a) and degradation efficiency (b).

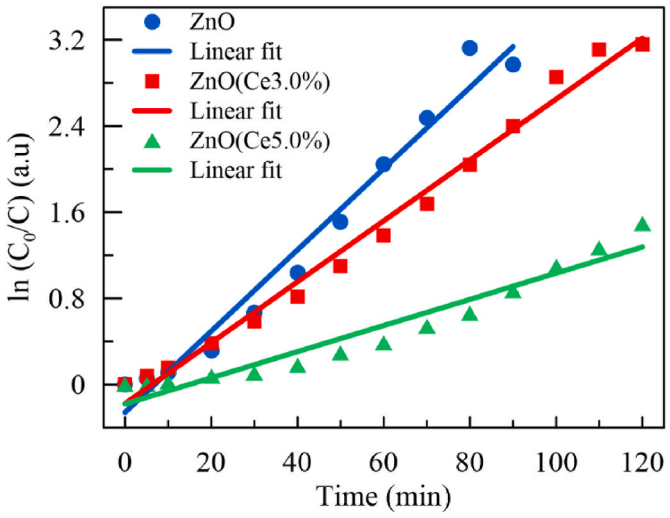

Fig. 13. First-order kinetic plots of ZnO and Ce-doped ZnO nanostructures.

Table 2
Calculated parameters of the photocatalytic degradation process of undoped and Ce-doped ZnO nanostructures.

Sample	After 60 min of UV light exposure			After 120 min of UV light exposure		
	%η	TON	TOF (x10^{-3} min^{-1})	%η	TON	TOF (x10^{-3} min^{-1})
ZnO/Ce	87.0	0.22	3.66	94.9	0.24	2.00
ZnO/Ce (3.0 %Ce)	75.8	0.19	3.23	95.8	0.25	2.04
ZnO/Ce (5.0 %Ce)	32.2	0.08	1.38	77.6	0.20	1.67

* Number of molecules of MB was 9.379×10^{-7}.
in 30 mL solution.

in this study exhibit one of the highest photocatalytic efficiencies (96 %) for methylene blue degradation under UV light, with a significantly shorter irradiation time (120 min) compared to other dopants and light sources. This demonstrates the potential of the SILAR-based Ce-doped ZnO films as a cost-effective and efficient photocatalyst for environmental applications.

Table 3
A comparison of photocatalytic efficiencies of various doped metal oxide catalysts has been reported in the literature with different dyes and light sources. The Ce-doped ZnO nanostructures developed in this study exhibited the highest degradation efficiency for methylene blue under UV irradiation.

Light source	Dye	Dopant	%η[a]	Irradiation time (min)	Ref.
Mercury bulb	Methyl orange	Fe	~20	180	[90]
Sunlight	RB5	Fe	90	180	[91]
Xenon lamp	Orange G	Al	51	180	[92]
		Ni	8.6		
Solar light	Orange G	rGO	18	180	[93]
Xenon lamp	Orange G	Cu	20	180	[94]
Sunlight	Methylene blue	Ba	~76	180	[95]
	Amoxicillin		~14	180	
UV	Methylene blue	Cd	82.5	150	[96]
Sunlight	Methylene blue	Sr	94.8	–	[97]
UV	Methylene blue	Ag	75.8	180	[98]
UV	Methylene blue	Ce	95.8	120	In this work

[a] The optimal values have been tabulated in studies based on multiple parameters.

4. Conclusions

In summary, this study presents the synthesis of ZnO nanostructures with varying concentrations of Ce, achieved through the SILAR method. The investigation focused on the morphological, structural, optical, and electrical properties of ZnO nanostructures and their photocatalytic activity. SEM images confirmed that ZnO nanoparticles were densely dispersed on the surfaces and showed a hexagonal flower shape morphology for the nanoparticles. XRD results show that Ce doping was successfully incorporated into the ZnO lattice, and the average crystal size ranged from 57.3 to 60.3 nm when the concentration was increased from 0.0 % to 5.0 %. UV–Vis results indicate that the energy band gap of the synthesized ZnO structures decreased from 3.24 eV to 3.05 eV with the change in Ce concentration. It was concluded that Ce doping affects the electrical properties of ZnO thin films. Total resistance values decrease with Ce doping, with the lowest resistance observed at 3.0 % Ce content. The increase in surface roughness determined by doping with AFM is supported by electrical measurement results. This effect is observed, especially in specific contact resistance. Because the rise in Ce doping in ZnO thin films also increases the specific contact resistance, adjustments in production parameters may be necessary to optimize performance. In addition, the total resistance values decrease with Ce doping, the lowest resistance is observed at 3.0 % Ce, and its value slightly increases at doping above this rate. However, it is still lower than the undoped ZNO. Similar behavior is observed in the catalytic activity. ZnO nanostructures doped with 3.0 % Ce exhibited improved catalytic activity, with enhanced percentage η and TOF values. After 120 min of UV light exposure, the %η reached 95.8 for the 3.0 % Ce-doped sample. However, when the Ce doping level was increased to 5.0 %, excessive metal ions negatively impacted the formation of e^-/h^+ pairs, decreasing TON and TOF values. These results suggest that there is an optimal Ce doping level (~3.0 %) at which the balance between charge separation and crystallographic/electronic disorder is maximized, leading to the best photocatalytic performance. Excessive doping, in contrast, introduces undesirable effects that outweigh the benefits of band gap reduction. In conclusion, Ce-doped ZnO nanostructures exhibit enhanced photocatalytic efficiency under UV light, and the material system demonstrates promise for environmental applications such as dye degradation. However, further investigations under visible light conditions are necessary to fully leverage the band gap narrowing effect and confirm the practical potential of these nanostructures for solar-driven photocatalysis.

CRediT authorship contribution statement

Ümmühan Akın: Writing – review & editing, Data curation, Investigation. **Hamide Avcı:** Writing – review & editing, Data curation, Investigation. **Raşit Aydın:** Supervision, Formal analysis, Methodology, Writing – review & editing, Investigation, Data curation. **Abdullah Akkaya:** Writing – review & editing, Data curation, Investigation. **Osman Kahveci:** Investigation, Data curation, Writing – review & editing. **Bünyamin Şahin:** Supervision, Data curation, Investigation, Methodology. **Enise Ayyıldız:** Methodology, Data curation, Investigation.

Declaration of competing interest

The authors declare that they have no known competing financial interests or personal relationships that could have appeared to influence the work reported in this paper.

Acknowledgments

This work was supported by the Selcuk University Scientific Research Projects Coordination Unit (BAP) (Project No: 24401003).

Data availability

Data will be made available on request.

References

[1] J. Iyyappan, B. Gaddala, R. Gnanasekaran, M. Gopinath, D. Yuvaraj, V. Kumar, Critical review on wastewater treatment using photo catalytic advanced oxidation process: role of photocatalytic materials, reactor design and kinetics, Case Stud. Chem. Environ. Eng. 9 (2024) 100599.
[2] N.H. Solangi, R.R. Karri, S.A. Mazari, N.M. Mubarak, A.S. Jatoi, G. Malafaia, A. K. Azad, MXene as emerging material for photocatalytic degradation of environmental pollutants, Coord. Chem. Rev. 477 (2023) 214965.
[3] K.S. Randhawa, Photocatalytic degradation of pollutants using advanced ceramics: materials, mechanism, synthesis, and applications, J. Inorg. Organomet. Polym. Mater. 34 (2024) 3931–3956.
[4] B. Tryba, P. Rychtowski, A. Markowska-Szczupak, J. Przepiórski, Photocatalytic decomposition of acetaldehyde on different TiO2-Based materials: a review, Catalysts 10 (12) (2020) 1464.
[5] S. Balu, D. Ganapathy, S. Arya, R. Atchudan, A.K. Sundramoorthy, Advanced photocatalytic materials based degradation of micropollutants and their use in hydrogen production – a review, RSC Adv. 14 (2024) 14392–14424.
[6] S. Marouch, N. Benbellat, A. Duran, E. Yilmaz, Nanoclay- and TiO2 nanoparticle-modified Poly(N-vinyl pyrrolidone) hydrogels: a multifunctional material for application in photocatalytic degradation and adsorption-based removal of organic contaminants, ACS Omega 7 (2022) 35256–35268.
[7] M. Ikram, M. Rashid, A. Haider, S. Naz, J. Haider, A. Raza, M.T. Ansar, M.K. Uddin, N.M. Ali, S.S. Ahmed, M. Imran, S. Dilpazir, Q. Khan, M. Maqbool, A review of photocatalytic characterization, and environmental cleaning, of metal oxide nanostructured materials, Sustain. Mater. Technol. 30 (2021) e00343.
[8] P. Muthukumar, D. Yuvapriya, D. Selvakumar, S. Niranjana Sri, N. Saisubramanian, M. Pannipara, A.G. Al-Sehemi, S. Philip Anthony, Plasmonic nanoparticles doped metal oxide hybrid materials for efficient photocatalytic dye degradation and strong anti-biofilm activity, Mater. Sci. Eng., B 296 (2023) 116688.
[9] R. Aydin, B. Şahin, The role of Triton X-100 as a surfactant on the CdO nanostructures grown by the SILAR method, J. Alloys Compd. 705 (2017) 9–13.
[10] A.E. Alprol, A.T. Mansour, A.M. Abdelwahab, M. Ashour, Advances in green synthesis of metal oxide nanoparticles by marine algae for wastewater treatment by adsorption and photocatalysis techniques, Catalysts 13 (5) (2023) 888.
[11] K. Prakruthi, M.P. Ujwal, S.R. Yashas, B. Mahesh, N. Kumara Swamy, H. P. Shivaraju, Recent advances in photocatalytic remediation of emerging organic pollutants using semiconducting metal oxides: an overview, Environ. Sci. Pollut. Control Ser. 29 (2022) 4930–4957.
[12] K. Sasikumar, H. Ju, Recent advances in vanadate-based materials for photocatalytic hydrogen production, Molecules 30 (4) (2025) 789.
[13] S. Azizi, M. Sellam, N. Mesri, T. Sehili, N. Gherraf, Photocatalytic degradation of methyl green by doped zinc oxide thin layers under solar irradiation, J. Photochem. Photobiol. Chem. 453 (2024) 115681.
[14] S. Ahmad, M. Usman, M. Hashim, A. Ali, R. Shah, N.U. Rahman, Investigation of optical and dielectric properties of nickel-doped zinc oxide nanostructures prepared via coprecipitation method, Nanomater. Nanotechnol. 2024 (2024) 8330886.
[15] P.K. Shihabudeen, S. Gupta, M.Y. Notash, J.J. Sardroodi, S.-W. Chiu, N.-H. Tai, K.-T. Tang, Chemiresistive room temperature NO2 sensor based on nitrogen doped zinc oxide nanowires, Sensor. Actuator. B Chem. 394 (2023) 134438.
[16] M. Asif, M. Fakhar-e-Alam, M. Tahir, F. Jamil, H. Sardar, J. Rehman, K.A. Dahlous, Synthesis, characterization, and evaluation of the antimicrobial and anticancer activities of zinc oxide and aluminum-doped zinc oxide nanocomposites, Pharmaceuticals 17 (9) (2024) 1216.
[17] R. Deep, T. Yoshida, Y. Fujita, Defects in nitrogen-doped ZnO nanoparticles and their effect on light-emitting diodes, Nanomaterials 14 (11) (2024) 977.
[18] Y. Hao, X. Liu, Z. Wang, H. Song, L. Wang, J. Zheng, H. Wang, L. Yan, C. Wei, Y. Yang, Robust and reliable organic dye-embedded zinc oxide nanocomposite phosphor with a broad spectrum and high efficiency enables an eco-friendly white laser light diode, ACS Sustain. Chem. Eng. 12 (2024) 6738–6747.
[19] F. Mechai, A. Al Shboul, M.O. Bensidhoum, H. Anabestani, M. Ketabi, R. Izquierdo, Influence of pH on room-temperature synthesis of zinc oxide nanoparticles for flexible gas sensor applications, Chemosensors 12 (5) (2024) 83.
[20] V. Kadam, C. Jagtap, T. Alshahrani, P. Lokhande, A. Al-Ahmed, S.P. Patole, F. Khan, H. Pathan, Synthesis and characterization of ZnO nanoparticles and their application in dye-sensitized solar cells, J. Mater. Sci. Mater. Electron. 34 (2023) 1864.
[21] A. Gupta, J.R. Saurav, S. Bhattacharya, Solar light based degradation of organic pollutants using ZnO nanobrushes for water filtration, RSC Adv. 5 (2015) 71472–71481.
[22] Y. Li, C. Liao, S.C. Tjong, Recent advances in zinc oxide nanostructures with antimicrobial activities, Int. J. Mol. Sci. 21 (22) (2020) 8836.
[23] A. Rajan, V. Gupta, K. Arora, Thickness dependent ultraviolet photoconductivity studies on sol-gel derived zinc oxide (ZnO) films, Mater. Today Commun. 35 (2023) 105507.
[24] L. Ruilin, K.Y. Yee, N.A. Salleh, B. Deghfel, Z. Zakaria, M.K. Yaakob, H.R. Ong, W. Rahiman, H. Akbulut, D. Wang, S. Kheawhom, A.A. Mohamad, Hydrothermal synthesis of manganese doped zinc oxide wurtzite nanoparticles for supercapacitors – a brief review, Inorg. Chem. Commun. 170 (2024) 113311.
[25] V. Saravade, Z. Manzoor, A. Corda, C. Zhou, I. Ferguson, N. Lu, Optical and structural properties of manganese-doped zinc oxide grown by metal-organic chemical vapor deposition, Adv. Opt. Mater. 9 (2021) 2100096.
[26] B. Ranjithkumar, H.B. Ramalingam, E.R. Kumar, C. Srinivas, G. Magesh, C. S. Rahale, N.M. El-Metwaly, B.C. Shekar, Natural fuels (Honey and Cow urine) assisted combustion synthesis of zinc oxide nanoparticles for antimicrobial activities, Ceram. Int. 47 (2021) 14475–14481.
[27] A.H. Noroozi, M. Sadeghi, A.A. Tehrani, P. Sarabadani, S. Rajabaifar, M. Mirzaee, Synthesis and characterization of zinc oxide nano-particles by solid state chemical reaction method, J. Cluster Sci. 24 (2013) 757–770.
[28] A. Akkaya, O. Kahveci, R. Aydın, B. Şahin, Amplifying main physical characteristics of CuO films using ascorbic acid as the reducer and stabilizer agent, Appl. Phys. A 127 (2021) 911.
[29] M.T. Khan, K.H. Prasad, A. Khan, M. Shkir, Enhancement of photodetector performance of aluminum-doped zinc oxide thin films fabricated via SILAR method: structural, optical, and electrical analysis, Inorg. Chem. Commun. 169 (2024) 112973.
[30] E. Arulkumar, S. Thanikaikarasan, S. Rajkumar, W. Wondimu, Influence of solution pH dependency on structure, optical with photoelectrochemical characteristics of SILAR deposited copper oxide thin films, Heliyon 10 (2024) e33579.
[31] R. Aydin, B. Sahin, Li:Ce co-doped CdO films synthesized by SILAR method: effects of rare earth element Ce content on the physical attributes, Ceram. Int. 44 (2018) 22249–22254.
[32] A.S. Sá, I.S. de Lima, L.M. Honório, M.B. Furtini, J.K.D. de Souza, F.E.P. dos Santos, H.M. Barreto, T.G. Tabuti, E.C. da Silva-Filho, E.R. Triboni, J.A. Osajima, ROS-mediated antibacterial response of ZnO and ZnO containing cerium under light, Chem. Pap. 76 (2022) 7051–7060.
[33] N.V. Petrakova, Y.O. Zobkova, V.S. Komlev, A.A. Ashmarin, A.S. Lysenkov, V. A. Volchenkova, S.M. Barinov, M.A. Sadovnikova, F.F. Murzakhanov, M. R. Gafurov, E.A. Kudryavtsev, S.A. Kozyukhin, A.L. Trigub, A.V. Rogachev, Synthesis and characterization of luminescent cerium-doped hydroxyapatite, Ceram. Int. 50 (2024) 20905–20916.
[34] S.M.A. Nsar, Z. Hassan, K.Y. Cheong, W. Foong Lim, A review on potential use of cerium oxide and doped cerium oxide as high dielectric constant seed layers for overgrowth of cerium oxide nanostructures, Mater. Res. Express 11 (2024) 062003.
[35] L. Wang, Z. Ji, J. Lin, P. Li, Preparation and optical and photocatalytic properties of Ce-doped ZnO microstructures by simple solution method, Mater. Sci. Semicond. Process. 71 (2017) 401–408.
[36] N. Fifere, A. Airinei, D. Timpu, A. Rotaru, L. Sacarescu, L. Ursu, New insights into structural and magnetic properties of Ce doped ZnO nanoparticles, J. Alloys Compd. 757 (2018) 60–69.
[37] S. Chattopadhyay, A. Kumawat, K.P. Misra, N. Halder, A. Bandyopadhyay, A. Antony, A. Rao, P. Poornesh, J. Jedryka, K. Ozga, B. Kucharska, R.D.K. Misra, Micro-strain administered SHG intensity enhancement by heavy Ce doping in co-precipitated ZnO nanoparticles, Mater. Sci. Eng., B 266 (2021) 115041.
[38] J.-Q. Wen, J.-M. Zhang, Z.-G. Qiu, X. Yang, Z.-Q. Li, The investigation of Ce doped ZnO crystal: the electronic, optical and magnetic properties, Phys. B Condens. Matter 534 (2018) 44–50.
[39] E.Y. Rodriguez-Mena, L.A. Alcalá-Varilla, J.D. Ortiz-Romero, First-principles study of the consequences of cerium doping on the photocatalytic activity of zinc oxide, Int. J. Mol. Sci. 25 (23) (2024) 13033.
[40] B.W. Hoogendoorn, B.K. Birdsong, A.J. Capezza, V. Ström, Y. Li, X. Xiao, R. T. Olsson, Ultra-low concentration of cellulose nanofibers (CNFs) for enhanced nucleation and yield of ZnO nanoparticles, Langmuir 38 (2022) 12480–12490.
[41] K. Quester, M. Avalos-Borja, E. Castro-Longoria, Biosynthesis and microscopic study of metallic nanoparticles, Micron 54–55 (2013) 1–27.
[42] S. Borbón, S. Lugo, D. Pourjafari, N. Pineda Aguilar, G. Oskam, I. López, Open-Circuit Voltage (VOC) Enhancement in TiO2-Based DSSCs: incorporation of ZnO Nanoflowers and Au Nanoparticles, ACS Omega 5 (2020) 10977–10986.
[43] S. Tekin, B. Unveroglu Abdioglu, C. Bozer, I. Karaduman Er, S. Acar, Enhanced linear and nonlinear optical characteristics of cerium (Ce) doped ZnO film, Ceram. Int. 51 (2025) 5309–5328.
[44] C.K. Kasar, J.P. Bange, D.S. Patil, Effect of cerium composition on optical and structural properties of cerium doped ZnO nanowires, J. Mater. Sci. Mater. Electron. 28 (2017) 11217–11221.
[45] Y.N. Wang, J. Li, Cerium modified rod-like ZnO graphene complex and its photocatalytic properties under visible-light irradiation, Opt. Mater. 108 (2020) 110203.
[46] A. Tounsi, R. Khalfi, D. Talantikite-Touati, H. Merzouk, A. Souici, Characterization of cerium-doped zinc sulfide thin films synthesized by sol–gel method, Appl. Phys. A 128 (2022) 280.
[47] M. Gharibshahi, Physical properties of cerium doped-yttrium iron garnet ultrathin films for photovoltaic application, Ceram. Int. 45 (2019) 24437–24445.
[48] M. El Jouad, M. Alaoui Lamrani, Z. Sofiani, M. Addou, T. El Habbani, N. Fellahi, K. Bahedi, L. Dghoughi, A. Monteil, B. Sahraoui, S. Dabos, N. Gaumer, Roughness effect on photoluminescence of cerium doped zinc oxide thin films, Opt. Mater. 31 (2009) 1357–1361.

[49] M. Shkir, J. Hakami, M. Milon Hossain, N.S. Awwad, A. Khan, Excellent photo-detection properties of cerium doped ZnO device fabricated by spray pyrolysis technique, Inorg. Chem. Commun. 140 (2022) 109439.
[50] S. Karakaya, L. Kaba, Nanoflower-like cerium-doped ZnO photocatalyst deposited by spray pyrolysis for the degradation of methylene blue dye, Mater. Today Sustain. 27 (2024) 100875.
[51] A.A. Barzinjy, H.H. Azeez, Green synthesis and characterization of zinc oxide nanoparticles using Eucalyptus globulus labill. leaf extract and zinc nitrate hexahydrate salt, SN Appl. Sci. 2 (2020) 991.
[52] I. Ahmad, M.S. Akhtar, E. Ahmed, M. Ahmad, Aluminium and cerium co-doped ZnO nanoparticles: facile and inexpensive synthesis and visible light photocatalytic performances, J. Rare Earths 39 (2021) 151–159.
[53] S.P. Meshram, P.V. Adhyapak, S.K. Pardeshi, I.S. Mulla, D.P. Amalnerkar, Sonochemically generated cerium doped ZnO nanorods for highly efficient photocatalytic dye degradation, Powder Technol. 318 (2017) 120–127.
[54] A. Akkaya, E.K. Sarıkaya, O. Kahveci, R. Aydın, B. Şahin, E. Ayyıldız, Hyaluronic acid mediated ZnO-NPs: in relation to electrical and photocatalytic activity for dye degradation, J. Alloys Compd. 1005 (2024) 175861.
[55] Y. Slimani, A. Khan, R. Sivakumar, M. Nawaz, A. Thakur, Synergistic impact of lanthanum and cerium co-doping ZnO for improved photocatalytic rhodamine B degradation efficiency under UV light, J. Mol. Struct. 1322 (2025) 140366.
[56] P. Pandey, R. Kurchania, F.Z. Haque, Structural, diffused reflectance and photoluminescence study of cerium doped ZnO nanoparticles synthesized through simple sol–gel method, Optik 126 (2015) 3310–3315.
[57] R. Bakkiyaraj, M. Balakrishnan, R. Subramanian, Synthesis, structural characterisation, optical studies of CeO_2 nanoparticles and its cytotoxic activity synthesis, structural characterisation, optical studies of CeO_2 nanoparticles and its cytotoxic activity, Mater. Res. Innov. 21 (6) (2016) 351–357.
[58] Z. Nazir Kayani, W. Chaudhry, R. Sagheer, S. Riaz, S. Naseem, Effect of Ce doping on crystallite size, band gap, dielectric and antibacterial properties of photocatalyst copper oxide Nano-structured thin films, Mater. Sci. Eng., B 283 (2022) 115799.
[59] G.L. Bhagyalekshmi, A.P.N. Sha, D.N. Rajendran, Temperature-independent photoluminescence response in zno:ce nanophosphor, Bull. Mater. Sci. 40 (2017) 1429–1434.
[60] A.K. Soğuksu, S. Kerli, Y. Kavun, Ü. Alver, Synthesis and characterizations of Ce-doped ZnO thin films for radiation shielding, Opt. Mater. 148 (2024) 114941.
[61] J. Tauc, Optical properties of amorphous semiconductors, in: J. Tauc (Ed.), Amorphous and Liquid Semiconductors, Springer US, Boston, MA, 1974, pp. 159–220.
[62] H. Parangusan, D. Ponnamma, M.A.A. Al-Maadeed, Effect of cerium doping on the optical and photocatalytic properties of ZnO nanoflowers, Bull. Mater. Sci. 42 (2019) 179.
[63] J. Iqbal, X. Liu, H.-C. Zhu, C. Pan, Y. Zhang, D. Yu, R. Yu, Trapping of Ce electrons in band gap and room temperature ferromagnetism of Ce4+ doped ZnO nanowires, J. Appl. Phys. 106 (2009) 83515, 083515.
[64] N. Djaja, R. Saleh, Characteristics and photocatalytics activities of Ce-Doped ZnO nanoparticles, Mater. Sci. Appl. 4 (2013) 145–152.
[65] N. Sharma, P. Sahay, Effect of (Ce, Dy) co-doping on the microstructural, optical and photoluminescence characteristics of solution combustion synthesized ZnO nanoparticles, Luminescence 38 (2023).
[66] T.B. Ivetic, M.R. Dimitrievska, I.O. Gúth, L. Dacanin, S.R. Lukic-Petrovic, Structural and optical properties of europium-doped zinc oxide nanopowders prepared by mechanochemical and combustion reaction methods, J. Res. Phys. 36 (2012) 43.
[67] I.T. Liu, M.-H. Hon, L.G. Teoh, The preparation, characterization and photocatalytic activity of radical-shaped CeO2/ZnO microstructures, Ceram. Int. 40 (2014) 4019–4024.
[68] G. Vijayaprasath, P. Soundarrajan, G. Ravi, Synthesis of ZnO nanosheets morphology by Ce doping for photocatalytic activity, J. Electron. Mater. 48 (2019) 684–695.
[69] C.-J. Chang, C.-Y. Lin, M.-H. Hsu, Enhanced photocatalytic activity of Ce-doped ZnO nanorods under UV and visible light, J. Taiwan Inst. Chem. Eng. 45 (2014) 1954–1963.
[70] D.K. Sharma, K.K. Sharma, V. Kumar, A. Sharma, Effect of Ce doping on the structural, optical and magnetic properties of ZnO nanoparticles, J. Mater. Sci. Mater. Electron. 27 (2016) 10330–10335.
[71] Y. Liang, N. Guo, L. Li, R. Li, G. Ji, S. Gan, Preparation of porous 3D Ce-doped ZnO microflowers with enhanced photocatalytic performance, RSC Adv. 5 (2015) 59887–59894.
[72] C.K. Kasar, U.S. Sonawane, J.P. Bange, D.S. Patil, Optical and structural properties of nanoscale undoped and cerium doped ZnO with granular morphology, J. Mater. Sci. Mater. Electron. 27 (2016) 11885–11889.
[73] L.-Y. Wang, M.-Q. Wang, C.-B. Yao, H.-T. Yin, X.-J. Liu, B.-Y. Shi, Two-step strategy, growth mechanism and optical properties of plasmonic Ag-modified ZnO nanomaterials, RSC Adv. 12 (2022) 3013–3026.
[74] B. Sahin, A. Acar, T. Kaya, Simple and low-cost synthesis of Al-doped ZnO/CuO composite nanowires for highly efficient hydration level sensing, Ceram. Int. 47 (2021) 11405–11414.
[75] Y.N. Wang, J. Li, Q. Wang, The performance of daylight photocatalytic activity towards degradation of MB by the flower-like and approximate flower-like complexes of graphene with ZnO and cerium doped ZnO, Optik 204 (2020) 164131.
[76] S. Mala, H.K.E. Latha, A. Udayakumar, Influence of post-deposition annealing temperature on structural and electrical properties of TiW contact thin films, J. Kor. Phys. Soc. 83 (2023) 194–199.
[77] A. Akkaya, O. Kahveci, B. Şahin, E. Ayyıldız, Simultaneously-doping of HfO_2 thin films by Ni with sputtering technique and effect of post annealing on structural and electrical properties, Phys. B Condens. Matter 665 (2023) 415034.
[78] B. Sultan, Q. Drmosh, E. Shalaan, H. Al-Jawhari, Engineering the contact resistance of copper/copper oxide via inserting a mediated molybdenum trioxide layer, Solid State Electron. 210 (2023) 108800.
[79] D.-Y. Lee, W.-S. Ko, K.-N. Kim, J.-H. Byun, E.-G. Kim, S.-Y. Kwon, G.-W. Lee, Analysis of metal and zinc oxide semiconductor interface resistance using transmission line method, Solid State Electron. 216 (2024) 108916.
[80] L. Brillson, Y. Lu, ZnO schottky barriers and ohmic contacts, J. Appl. Phys. 109 (2011) 121301, 121301.
[81] B. Dong, X. Yu, Z. Dong, X. Yang, Y. Wu, Facile synthesis of ZnO nanoparticles for the photocatalytic degradation of methylene blue, J. Sol. Gel Sci. Technol. 82 (2017) 167–176.
[82] T. Munawar, F. Iqbal, S. Yasmeen, K. Mahmood, A. Hussain, Multi metal oxide NiO-CdO-ZnO nanocomposite–synthesis, structural, optical, electrical properties and enhanced sunlight driven photocatalytic activity, Ceram. Int. 46 (2020) 2421–2437.
[83] S. Harish, J. Archana, M. Sabarinathan, M. Navaneethan, K.D. Nisha, S. Ponnusamy, C. Muthamizhchelvan, H. Ikeda, D.K. Aswal, Y. Hayakawa, Controlled structural and compositional characteristic of visible light active ZnO/CuO photocatalyst for the degradation of organic pollutant, Appl. Surf. Sci. 418 (2017) 103–112.
[84] O. Kahveci, A. Akkaya, E.K. Sarıkaya, M. Çanlı, R. Aydın, B. Şahin, E. Ayyıldız, Construction of unary and ternary ZnO–CuO–CdO composite thin films and comprehensive analysis of their optical, electrical, and photocatalytic performance, J. Alloys Compd. 997 (2024) 174827.
[85] A. Tekin, R. Aydın, Ü. Akın, O. Kahveci, A. Akkaya, H. Kara, B. Şahin, Nanoscale engineering of Sr-doped ZnO nanorods/CuO nanocomposites for the photocatalytic treatment of methylene blue pollutant, Mater. Chem. Phys. 343 (2025) 131009.
[86] F. Rahman, M.A. Patwary, M. Siddique, M. Haque, B. Akter, R. Rashid, M.A. Haque, A. Uddin, Green synthesis of zinc oxide nanoparticles using Cocos nucifera leaf extract: characterization, antimicrobial, antioxidant and photocatalytic activity, R. Soc. Open Sci. 9 (2022).
[87] S. Kozuch, J.M.L. Martin, "Turning Over" definitions in catalytic cycles, ACS Catal. 2 (2012) 2787–2794.
[88] L. Gomathi Devi, R. Shyamala, Photocatalytic activity of SnO2–α-Fe_2O_3 composite mixtures: exploration of number of active sites, turnover number and turnover frequency, Mater. Chem. Front. 2 (2018) 796–806.
[89] C.-L. Chiang, K.-S. Lin, H.-W. Chuang, Direct synthesis of formic acid via CO_2 hydrogenation over Cu/ZnO/Al_2O_3 catalyst, J. Clean. Prod. 172 (2018) 1957–1977.
[90] K.A. Isai, V.S. Shrivatava, Photocatalytic degradation of methyl orange using ZnO and Fe doped ZnO: a comparative study, Iran. J. Catal. 9 (2024).
[91] M. Mohsin, I.A. Bhatti, A. Ashar, A. Mahmood, Maryam, Q.u. Hassan, M. Iqbal, Fe/ZnO@ceramic fabrication for the enhanced photocatalytic performance under solar light irradiation for dye degradation, J. Mater. Res. Technol. 9 (2020) 4218–4229.
[92] I. Jellal, O. Daoudi, K. Nouneh, M. Boutamart, S. Briche, M. Fahoume, J. Naja, Comparative study on the properties of Al- and Ni-doped ZnO nanostructured thin films grown by SILAR technique: application to solar photocatalysis, Opt. Quant. Electron. 55 (2023) 620.
[93] I. Jellal, N. Khalid, H. Rhizlane, B. Mustapha, B. Samir, A. Mohammed, P. Gael, B. Mimouna, J, Naja, Enhanced visible-light photocatalytic activity of rGO-ZnO composite thin films prepared by SILAR method, Adv. Mater. Proc. Technol. 9 (2023) 1045–1060.
[94] I. Jellal, O. Daoudi, K. Nouneh, M. Boutamart, S. Briche, G. Plantard, M. Fahoume, J. Naja, Successive ionic layer adsorption and reaction (SILAR) synthesis of micro-structured Cu-doped ZnO thin films with enhanced photocatalytic activity, J. Mater. Sci. Mater. Electron. 34 (2023) 672.
[95] H. Barkat, E. Guettaf Temam, H. Ben Temam, N. Mokrani, S. Rahmane, M. Althamthami, Thickness-dependent photocatalytic performance and wettability of barium-doped ZnO thin films synthesized via SILAR technique. Transition Metal Chemistry, 2025.
[96] M. Sathya, G. Selvan, M. Karunakaran, K. Kasirajan, S. Usha, M. Logitha, S. Prabakaran, P. Baskaran, Synthesis and characterization of cadmium doped on ZnO thin films prepared by SILAR method for photocatalytic degradation properties of MB under UV irradiation, Eur. Phys. J. Plus 138 (2023) 67.
[97] N. Mokrani, E. Guettaf Temam, H. Barkat, H. Ben Temam, S. Rahmane, M. Althamthami, Boosting photocatalytic stability: Hydrophilic Sr-doped ZnO thin films prepared via the SILAR method for enhanced performance over multiple cycles, Phys. Scripta 99 (2024) 0959a0954.
[98] M. Sathya, G. Selvan, K. Kasirajan, S. Usha, P. Baskaran, M. Karunakaran, S.S. R. Inbanathan, Photocatalytic degradation properties of SILAR grown ZnO:Ag thin films: investigation on the effect of Ag loading, Braz. J. Phys. 52 (2021) 23.